

Multifunctional Optoelectronics via Harnessing Defects in Layered Black Phosphorus

Taimur Ahmed,* Sruthi Kuriakose, Sherif Abbas, Michelle J. S. Spencer, Md. Aatur Rahman, Muhammad Tahir, Yuerui Lu, Prashant Sonar, Vipul Bansal, Madhu Bhaskaran, Sharath Sriram, and Sumeet Walia*

Layered black phosphorus (BP), a promising 2D material, tends to oxidize under ambient conditions. While such defective BP is typically considered undesirable, defect engineering has in fact been exploited in contemporary materials to create new behaviors and functionalities. In this spirit, new opportunities arising from intrinsic defect states in BP, particularly through harnessing unique photoresponse characteristics, and demonstrating three distinct optoelectronic applications are demonstrated. First, the ability to distinguish between UV-A and UV-B radiations using a single material that has tremendous implications for skin health management is shown. Second, the same device is utilized to show an optically stimulated mimicry of synaptic behavior opening new possibilities in neuromorphic computing. Third, it is shown that serially connected devices can be used to perform digital logic operations using light. The underpinning photoresponse is further translated on flexible substrates, highlighting the viability of the technology for mechanically conformable and wearable systems. This demonstration paves the way toward utilizing the unexplored potential offered by defect engineering of 2D materials for applications spanning across a broad range of disciplines.

a direct bandgap even in the bulk state.^[1–4] Its thickness-dependent bandgap ranges from 0.3 eV for bulk to ≈ 2 eV for a monolayer.^[5,6] The strong light–matter coupling in BP renders it as an ideal 2D material for broadband photodetection covering spectral range from shorter wavelengths (deep UV) to infrared.^[7] However, one of the key limitations typically considered with BP is its tendency to spontaneously oxidize even under ambient conditions.^[8–12] This process either creates a myriad of defect states in BP that alter its optoelectronic characteristics or completely degrades BP rendering it unusable.^[7,13] Considering the emphasis on stability and retaining the pristine properties of this interesting 2D material, BP can now be successfully protected against ambient oxidation and/or degradation by employing a variety of strategies including surface encapsulation, functionalization, and modification.^[14–18]

While defects in BP are typically considered problematic, in contemporary areas of materials science, defect engineering has proven to be a simplistic pathway to create new behaviors and functionalities.^[19–21] Our current work exploits the potential of self-propagating defects in BP to create unique functional optoelectronic capabilities. The

1. Introduction

Among the family of elemental analogues of graphene, black phosphorus (BP) has emerged as a material of interest owing to its high hole mobility ($\approx 10^3$ cm² V⁻¹ s⁻¹) and the presence of

Dr. T. Ahmed, S. Kuriakose, M. A. Rahman, Prof. M. Bhaskaran,
Prof. S. Sriram, Dr. S. Walia
Functional Materials and Microsystems Research Group
and the Micro Nano Research Facility
RMIT University
Melbourne, VIC 3000, Australia
E-mail: taimur.ahmed@rmit.edu.au; sumeet.walia@rmit.edu.au

Dr. S. Abbas, Prof. M. J. S. Spencer
School of Science
RMIT University
Melbourne, VIC 3000, Australia


Dr. M. Tahir
Department of Physics
Colorado State University
Fort Collins, CO 80523, USA

Prof. Y. Lu
Research School of Engineering
College of Engineering and Computer Science
Australian National University
Canberra, ACT 2600, Australia

Prof. P. Sonar
School of Chemistry
Physics and Mechanical Engineering
Queensland University of Technology
2 George Street, Brisbane, QLD 4000, Australia

Prof. V. Bansal
Sir Ian Potter NanoBioSensing Facility
and NanoBiotechnology Research Laboratory
School of Science
RMIT University
Melbourne, VIC 3000, Australia

Dr. S. Walia
School of Engineering
RMIT University
Melbourne, VIC 3000, Australia

 The ORCID identification number(s) for the author(s) of this article can be found under <https://doi.org/10.1002/adfm.201901991>.

DOI: 10.1002/adfm.201901991

exciting optoelectronic behavior harnessed from defective BP in our study can only otherwise be achieved in other materials by applying altering-polarity gate fields that not only have significant effects on energy consumption but also make device operation significantly complex.^[22–24] Specifically, a defect-induced unique photoresponse is reported in our BP devices, wherein a reduction in the device conductivity is observed under the excitation of nonpolarized 365 nm light source, while an opposite behavior (increase in conductivity) is observed under a 280 nm excitation. This opposing photoresponse without the application of any alternating-polarity gate field opens exciting new applications that have not been demonstrated with any material system till date. We further harness this unusual photoresponse of defective BP to showcase three different applications.

First, we show that this material system is capable of effectively distinguishing between UV-A (365 nm) and UV-B (280 nm) parts of the electromagnetic spectrum. This finding has significant implications for epidermal health management and prevention of UV damage-induced melanoma, as UV-A and UV-B have very different effects on the human skin.^[25–27] Second, we show a simple optoelectronic synapse that can mimic the excitatory and inhibitory action potentials of biological synapses without relying on the need for simultaneously altering the polarity of the applied electric fields. Third, we show optically stimulated fundamental logic operations in

our proof-of-concept integrated BP devices. Demonstration of light-stimulated synapses and logic operations from a single material system offers new synergies to develop novel devices for future photonic neuromorphic circuits and artificial sensory organs, such as artificial retina. Furthermore, we demonstrate that these unique optoelectronic characteristics of BP can be achieved on both a rigid complementary metal-oxide semiconductor-compatible platform as well as on flexible platforms rendering multifunctionality for wearable systems.

2. Results

2.1. Anisotropic Photoresponse of BP

In order to characterize the ambipolar optoelectronic properties of few-layer BP, flakes with different thicknesses are selected for fabricating devices (see the Experimental Section). **Figure 1a** shows an atomic force microscopy (AFM) topographic scan and height profile (Figure 1b) of ≈ 5.7 nm BP flake (corresponding to ten layers) selected for a representative device on a SiO₂/Si substrate (Figure 1c). Two pairs of metal electrodes are orthogonally patterned on the selected BP flakes, where an electrode pair (A–B) is patterned along the *x*-direction (armchair) and another electrode pair (C–D) along the *y*-direction (zigzag). Prior to the

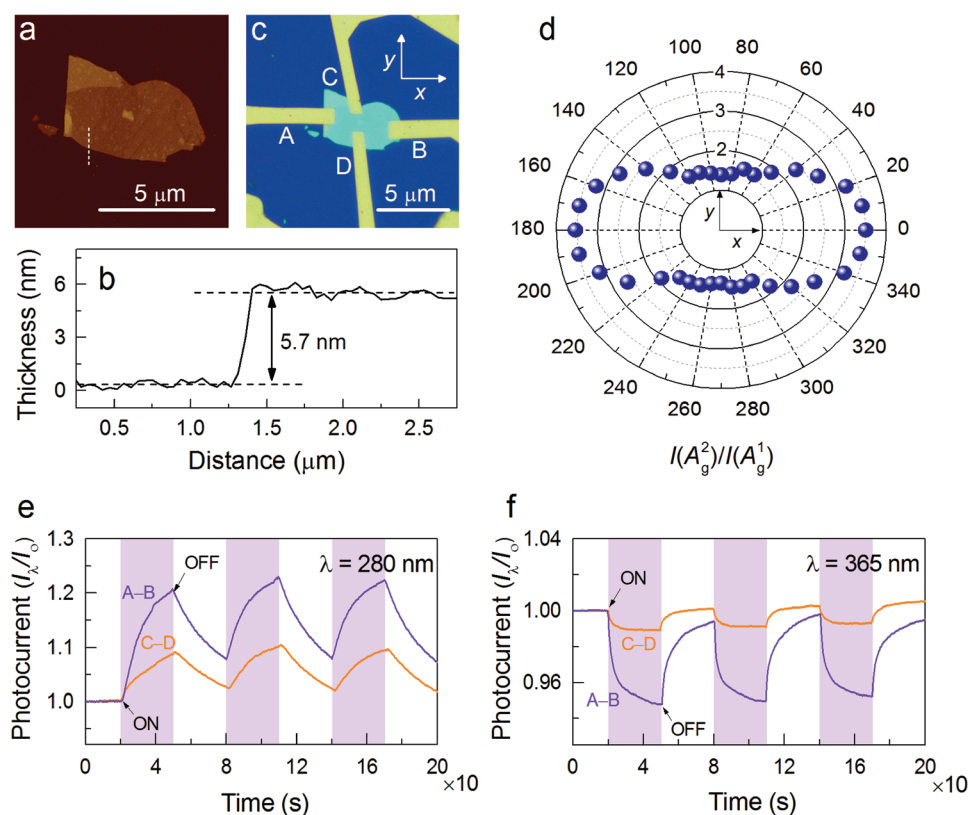


Figure 1. Few-layer BP device structure and anisotropic photoelectronic characterization. a) AFM topographic scan of the BP flake selected for a representative BP photonic device. b) Height profile of the BP flake measured along a line depicted on the topographic scan in (a) corresponds to 5.7 nm. c) Optical microscope photograph of a representative BP photonic device fabricated on a rigid SiO₂/Si substrate. Two sets of drain–source electrode pairs, namely, AB and CD, are fabricated orthogonally to each other and used for photoelectronic characterization. d) The ratio of Raman A_g² and A_g¹ peak intensity as a function of excitation laser polarization angles. Normalized transient photocurrent between A–B and C–D electrode pairs measured under pulsating e) UV-B ($\lambda = 280$ nm) and f) UV-A ($\lambda = 365$ nm) illuminations at power densities of 2 mW cm⁻² and a constant DC bias of 50 mV.

electrode fabrication, the BP crystal orientation is identified by the polarization-resolved Raman spectroscopy (Figure 1d), where the ratio of the A_g^2 and A_g^1 peak intensity is higher ($\approx 3.51 \pm 0.02$) along the x -direction than the y -direction ($\approx 1.35 \pm 0.03$). A detailed polarization-resolved Raman analysis is presented in Section S1 in the Supporting Information. Furthermore, anisotropy of the BP crystal is confirmed by the carrier mobility across the electrode pairs and solving low-energy $k \cdot p$ Hamiltonian, discussed in Section S1 in the Supporting Information.

Transient photoresponse of the representative device is acquired in the UV region of the light spectrum and along both electrode pairs at a constant DC bias of 50 mV. Figure 1e,f shows normalized transient photocurrent under the illumination of pulsating UV-B ($\lambda = 280$ nm) and UV-A ($\lambda = 365$ nm) excitation wavelengths, respectively, along the electrode pairs A–B and C–D. In more than 15 devices studied in this work, it is consistently observed that while the current increases on exposure to 280 nm, it shows an opposite (decreasing) trend on exposure to 365 nm wavelength. The relatively high photocurrent ($\approx 11\%$ for 280 nm and $\approx 4\%$ for 365 nm) along the A–B electrode pair than the C–D one can be associated with the in-plane optical anisotropy that allows higher absorption of the incident light in the armchair direction and dichroic photocurrent generation.^[6,28–30]

2.2. Mechanism of Photoresponse

In 2D systems, negative photoconductivity is typically associated with the bolometric effect.^[31–35] However, the unusual negative photocurrent observed in BP under long-wave UV (365 nm) excitation is intrinsically material related and is associated with the surface adsorbates.^[31,36] It is well known that BP in ambient conditions readily adsorbs oxygen and forms phosphorus oxide species across the crystal surface that can act as charge trap sites.^[8,9,11,15,36,37] These extrinsic trap sites act as scattering centers under light illumination and reduce the conductance of the device and, hence, are the origin of negative photocurrent. In contrast, Wu et al.^[38] previously reported positive photocurrent in BP phototransistors under 330 and 370 nm excitation wavelengths, operating under a negative gate voltage (-80 V) and high vacuum. The presence of electric field at BP/substrate interface can lead to the accumulation of photogenerated positively charge carriers (holes) at the interface resulting in an increase in photocurrent (between drain and source) on excitation. To gain an in-depth understanding of the origin of negative photocurrent under 365 nm excitation wavelength, we used a series of experimental characterizations coupled with density functional theory (DFT) calculations (discussed below).

Ambient oxidation of BP has been analyzed in several recently reported DFT investigations,^[8,10,39–43] where oxygen is predicted to spontaneously dissociate on BP, a process that is facilitated with reduction in the number of BP layers.^[44] The adsorption of atomic oxygen is reported to have a negative formation energy (E_f),^[41] which indicates that the incorporation of oxygen stabilizes some of the phosphorene defects. Of interest to the present work, Ziletti et al.^[40] predicted that metastable structures with adsorbed oxygen atoms exhibit localized defect levels. These levels, which are characterized by horizontal

discrete levels within the bandgap and do not endure significant dispersion, act as charge traps that diminish the conductance of BP under 365 nm illumination. The oxidation of defective BP, which can also be seen as a substitutional doping of BP with oxygen atoms, introduces localized defects in BP.^[41] As such, we expand the investigation of oxidized phosphorene by studying various oxidized structures and the nature of their induced defects (Section S2, Supporting Information). Since the oxygen dissociation reaction on the surface has a low energy barrier and high exothermicity,^[40] we consider chemical adsorption of oxygen on the surface of BP in our simulations.

Figure 2a shows the atomic structure of phosphorene after introducing an oxygen atom into the defective structure, while Figure 2c shows an oxidized structure (as in Figure 2a) stacked on two pristine phosphorene layers to form a trilayer structure. The localization of a defect level is indicated by the dispersiveness of the defect energy; that is, if the level in the band structure is a straight line, the defect will be spatially localized. The band structure of an oxidized phosphorene structure in Figure 2b, induced by incorporating an oxygen atom, shows a nearly straight defect level, which suggests that it is nearly localized. Furthermore, the defect levels induced in different oxidized structures are also nearly localized (Section S2, Supporting Information). The localization of the defect in the monolayer (Figure 2a,b) also persists in the case of the multilayer, as shown in the band structure in Figure 2d. The presence of localized defect levels in the oxidized structures at such low formation energies explains the observed negative photocurrent under 365 nm illumination: exposure to which causes the formation of oxidized defect structures that harbor localized defect levels and creating charge traps.

On the other hand, exposure to 280 nm wavelength light (having an energy of 4.4 eV, which is very close to the energy required to split a H_2 molecule) may give rise to a potential mechanism for the onset of photoconduction via the splitting of H_2 and H_2O molecules in ambient, resulting in passivation of oxygen sites in oxidized phosphorene and hence the introduction of carriers, which could subsequently lead to the photoconductivity within the sample (Section S2, Supporting Information). In addition to the H reduction, the increase in conductivity under high photon energy (>4 eV) excitation wavelengths (Section S5, Supporting Information) can also be explained by the ionization of defects.^[45–47] However, further theoretical investigation is required to validate the exact mechanism of reactions taking place under high photon energy irradiations, and this is the subject of ongoing work.

The energy-dispersive X-ray spectroscopy (EDS) and electron energy loss spectroscopic (EELS) analysis of our BP flakes show oxidation of as-exfoliated BP flakes and presence of a phosphorus oxide (PO_x) layer on the BP flakes (Section S4, Supporting Information). To assess the microstructure of PO_x layer in our BP devices, cross-sectional lamellae are prepared for transmission electron microscopy (TEM) analysis. Figure 3a shows a cross-sectional TEM image of a representative BP device with a structure of Au/Cr/BP/SiO₂/Si, where Au/Cr layers are patterned as electrical contacts. High-resolution TEM reveals the presence of ≈ 3 nm amorphous layers at the top Cr/BP and bottom BP/SiO₂ interfaces. The composition of these amorphous layers is identified by acquiring EELS O-K edge and

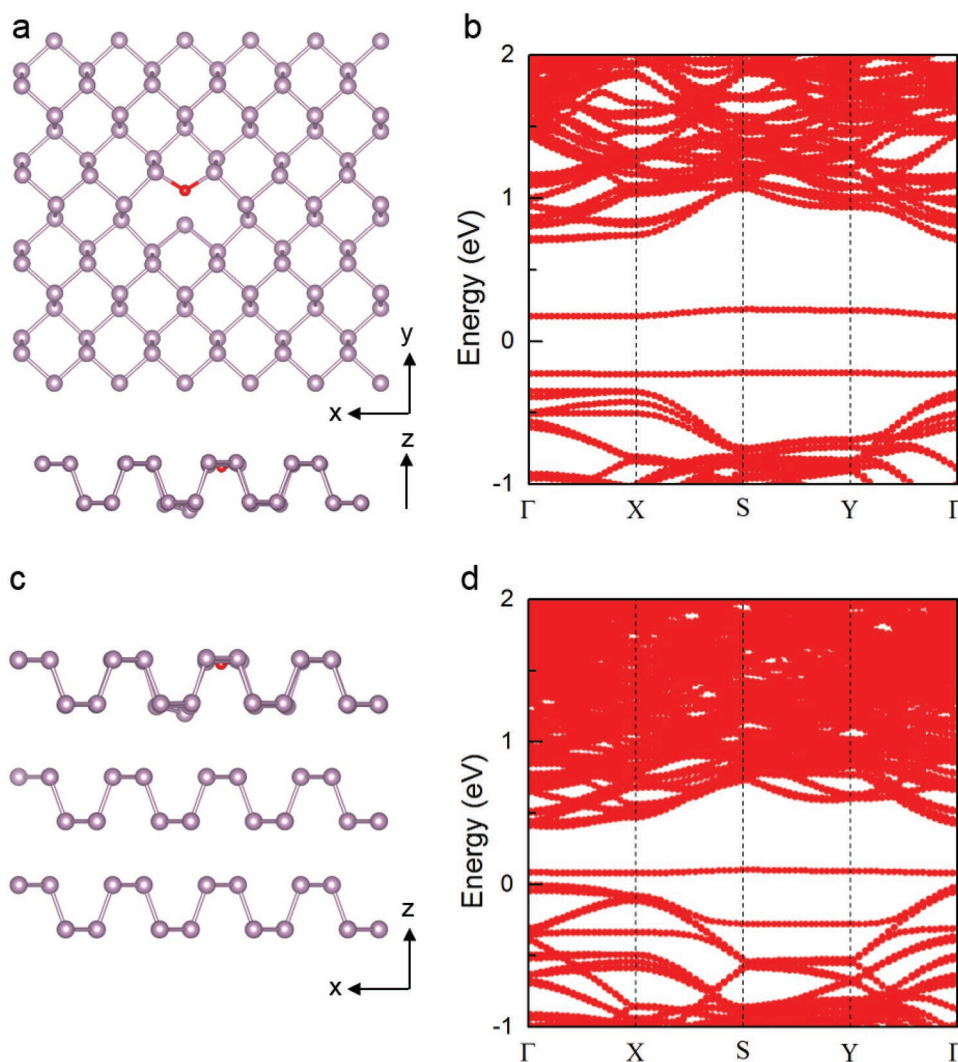


Figure 2. The density functional theory calculations for oxidized phosphorene. a) The atomic structure of defective phosphorene where one P atom is substituted with an O atom. The formation energy is calculated to be -2.43 eV per cell. b) The band structure of oxidized phosphorene corresponding to the structure in (a). c) The atomic structure of a trilayer system, where the top layer is the defect structure in (a). d) The band structure of the trilayer structure in (c).

P-L edge area maps (Figure 3b) of a region of interest, highlighted by an enclosed area in Figure 3a. The EELS area maps show oxygen content at the interfacial regions associated with the amorphous layers, indicating the presence of phosphorus oxide at the top and bottom interfaces of the BP device. Furthermore, the presence of oxygen content in the Cr layer can be attributed to the partial oxidation of Cr to chromium oxide during device fabrication.

Thermal treatment of 2D materials, including BP, is known to significantly reduce oxidation-related defects due to the evaporation of surface adsorbates.^[16,48,49] Based on this, it is expected that defect engineering by controlled thermal annealing of defective BP in an inert environment may tune the photoresponse of our devices. As such, we conduct a comparison between the photoresponse and material characteristics of thermally treated BP in an inert Ar environment and ambient exposed untreated BP. Figure 3c shows that an ambient exposed BP device exhibits negative photocurrent

under the illumination of 365 nm (also discussed in Figure 1) that changes to a positive photocurrent after the device is subjected to 150 °C for 60 min in Ar. This can be associated with the evaporation of surface adsorbates and associated reduction in carrier scattering centers during thermal treatment.^[16,48] On the other hand, the devices retain a positive photocurrent profile at 280 nm exposure. In situ Raman spectra (Figure 3d) of an ambient exposed flake show relatively small and broad peak in 800–900 cm^{-1} range that is associated with the Raman vibration modes of phosphorus oxide species.^[8,9,14] The presence of these oxide species is consistent with our cross-sectional TEM analyses. We note that the in situ Raman spectra of thermally treated BP flakes show significant reduction in the intensity of oxide peaks after annealing in Ar at 150 °C for 60 min. Furthermore, a relative change in the optical absorbance and morphology is observed after the thermal annealing of an ambient exposed BP flake (see Section S2 in the Supporting Information). Figure 3e shows a quantitative EDS comparison of a

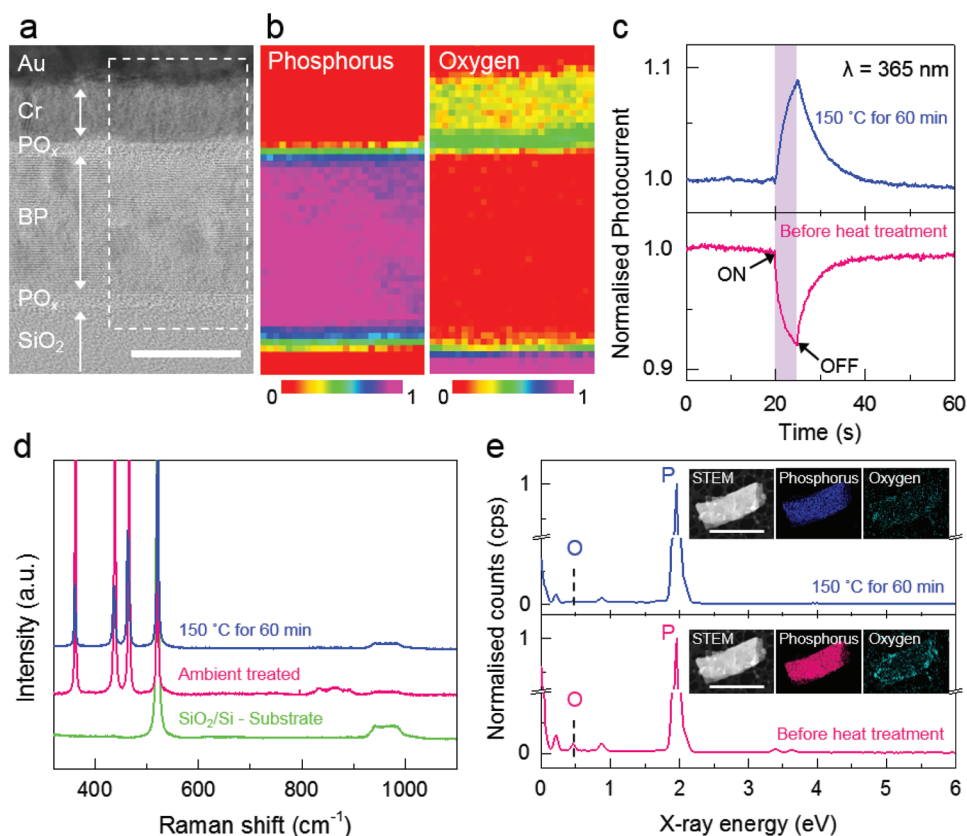


Figure 3. Role of defects on the photoresponse of few-layer BP. a) Cross-sectional TEM image of a representative BP device taken for the region under Au/Cr electrode. b) EELS area maps generated for a region of interest highlighted in (a) by taking O-K edge and P-L edge intensities of the collected spectra (at each pixel) after pre-edge background subtraction. c) Normalized photoresponse of a representative BP device under 365 nm illumination measured before and after subjected to 150 °C for 60 min in Ar. Photocurrents are measured under 4 and 9 mW cm⁻² of power density before and after thermal treatment, respectively. d) In situ Raman spectra of a BP flake subjected to ambient and 150 °C for 60 min in Ar. e) Normalized EDS spectra collected from a BP flake exfoliated on a TEM grid and exposed to ambient and heat treated at 150 °C for 60 min in Ar. Both spectra are normalized with phosphorus peak intensities. Insets show EDS area maps of the BP flake used for EDS analysis. Scale bar corresponds to 3 μm.

representative BP flake before and after thermal treatment at 150 °C in Ar for 60 min. The normalized X-ray energy spectra and EDS area maps (inset of Figure 3e) show that annealing in an inert Ar environment reduces oxygen content from 3.1 to 0.9 wt%, which is expected to be from the surface of BP flake. However, the presence of residual oxide observed after thermal treatment can be explained by the formation of a stable phase of phosphorus oxide (such as P₂O₅) as reported in the literature.^[48–50] The above-mentioned DFT simulations and characterizations reveal a vivid picture where localized charge trap sites induced by the dissociation of surface adsorbates define the conductance of BP based on the illumination energy. In addition, same photoresponse characteristics, i.e., positive photocurrent under 280 nm and negative photoresponse under 365 nm excitation wavelengths, in devices with Cr/Au and Ti/Au electrode junctions further support the discussion that BP is the functional component of photoresponse in our devices.

2.3. UV-A/B Discrimination

In order to systematically study the viability of BP devices to discriminate between UV-A and UV-B radiations, all

measurements are carried out through the electrode pairs along armchair direction. A broadband photoresponse of BP devices is also measured in the wavelength ranging between UV-C and visible light (455 nm) (Section S5, Supporting Information). However, we focus on UV-A and UV-B discrimination by our BP devices due to their technological and practical significance. It is observed that the photocurrent exhibits dependence on the incident power density of the UV-A and UV-B illuminations (Section S5, Supporting Information). **Figure 4a** shows the magnitude of power-dependent normalized photocurrent (I_{λ}/I_0) under UV-A and UV-B illumination densities ranging from 100 μW cm⁻² to 3 mW cm⁻². It is also observed that under a constant UV-A/B illumination power density, the photocurrent is independent of the BP crystal thicknesses ranging from ≈5.6 to ≈45 nm (selected in this work), as depicted in Figure 4b. This highlights a significant technological relevance that BP can effectively sense and discriminate UV-A/B radiations regardless of the crystal thickness.

Furthermore, their performance is quantitatively assessed by calculating figures of merit, including responsivity (R), external quantum efficiency (EQE), and specific detectivity (D^*) for both UV-A and UV-B wavelengths. The responsivity

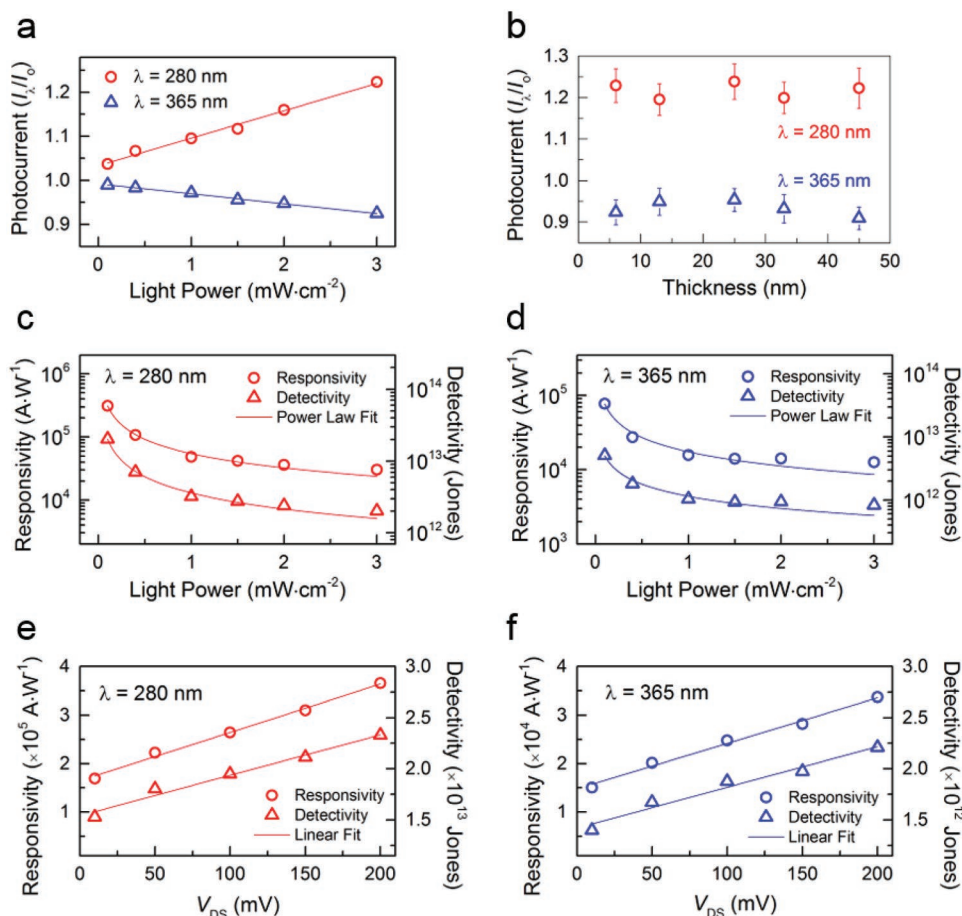


Figure 4. Photoresponse and UV discrimination of BP devices fabricated on rigid SiO₂/Si substrates. a) Normalized photocurrent as a function of UV-A and UV-B power densities, ranging from 0.1 to 3 mW cm⁻². Solid lines correspond to the linear fitting of the experimental data. b) Normalized photocurrent as a function of BP flake thickness selected for the BP devices. Incident power-dependent responsivity and detectivity for c) UV-B and d) UV-A illuminations. Solid lines correspond to the power law fitting of the experimental data. Drain-source voltage-dependent responsivity and detectivity for e) UV-B and f) UV-A illuminations. Solid lines correspond to the linear fitting of the experimental data.

that quantifies the photocurrent generated per unit power of the excitation wavelength on the effective area of a device is calculated by

$$R = \frac{\Delta I}{P_{\lambda} S} \quad (1)$$

where ΔI is the difference between the measured currents with (I_{λ}) and without (I_0) illumination, P_{λ} is the power density, and S is the effective area of the device. The external quantum efficiency defines the number of effective charge carriers generated per incident photon of the excitation wavelength and is calculated by the following equation:

$$EQE = \frac{\Delta I h \nu}{P_{\lambda} q} \quad (2)$$

where h is the Planck's constant, ν is the photon frequency, and q is the elemental charge. Furthermore, the specific detectivity describes the smallest detectable signal and is calculated by the following equation:

$$D^* = \frac{\sqrt{SB}}{NEP} \quad (3)$$

$$NEP = \frac{i_n}{R} \quad (4)$$

where B is the electrical bandwidth, NEP is the noise equivalent power, and i_n is the noise current. Among the three possible noise sources that may limit D^* are shot noise from dark current, thermal noise, and Johnson-Nyquist noise. The shot noise from the dark current can be considered as the main contributor here as the short-wavelength UV illuminations and low measurement voltages (10–200 mV) are used in our experiments.^[51] As such, Equation (3) can be simplified as

$$D^* = \frac{\sqrt{SR}}{\sqrt{2qI_{\text{Dark}}}} \quad (5)$$

Figure 4c,d presents the power-dependent responsivity (on left axes) and detectivity (on right axes) under UV-B and UV-A illuminations, respectively. The decrease in responsivity and

detectivity with increasing power density is consistent with the previously reported photodetectors.^[52,53] Generally, the photocurrent (I_λ) shows a linear dependence on the incident power density described by $I_\lambda \propto P_\lambda^\alpha$, where $\alpha = 1$ and is associated with the photoconductive effect, as seen in Figure 4a. However, charged trap states induced by the defects and surface and/or interfacial traps result in the photogating effect that introduces a sublinear dependence ($\alpha < 1$) on incident power density.^[54] The experimental data of power-dependent responsivity (Figure 4c,d) can be modeled by a power law dependence, i.e., $R \propto P_\lambda^{\alpha-1}$, where α is deduced to be ≈ 0.75 and ≈ 0.64 for UV-B and UV-A illuminations, respectively. This suggests that under the both illuminations, recombination of photogenerated carriers involves interaction with charged trap states introducing a sublinear dependence resulting in a prolonged lifetime and slow recovery (Section S6, Supporting Information).^[52,55] Also, comparatively slower response speed under 280 nm than 365 nm excitation wavelength can be associated with the higher photon energy (≈ 4.4 eV) and relatively higher absorbance, which excites large amount of charge carriers from lower valance band to conduction band and causes slower recombination.^[38] We suggest that an enhanced response speed (in milliseconds) under UV illumination can be achieved by controlling the defects, such as limiting the excessive surface oxidation by performing measurements in high vacuum and utilizing back gate field to trap defects at BP/substrate interface. Figure 4e,f shows the drain source bias (V_{DS})-dependent responsivity and specific detectivity under UV-B and UV-A illuminations, respectively, at a fixed power density of 0.4 mW cm^{-2} . Regardless of the excitation wavelength, both responsivity and specific detectivity exhibit linear dependence on V_{DS} , which can be associated with increasing carrier drift velocity as the bias is increased.^[56] Such V_{DS} -dependent responsivity is consistent with the previously reported photodetectors.^[38,56] In this work, the maximum responsivity of $3.6 \times 10^5 \text{ A W}^{-1}$ (with corresponding D^* of 2.3×10^{13} Jones and EQE of $1.6 \times 10^6\%$) is achieved for 280 nm illumination wavelength, whereas the responsivity of $3.3 \times 10^4 \text{ A W}^{-1}$ (with corresponding D^* of 2.2×10^{12} Jones and EQE of $1.5 \times 10^5\%$) is measured for 365 nm illumination wavelength. Relatively higher photoresponse (almost an order of magnitude) under 280 nm excitation wavelength compared to 365 nm can be attributed to the larger excitation energy supplied by higher photon energy of the shorter illumination wavelength. A comparison of figures of merit shows that the responsivity and detectivity reported in this work are the highest reported for a UV detector based on any 2D material (Table S1 in Section S7 of the Supporting Information). The operational performance in terms of cyclic endurance and time stability of BP devices is also evaluated. The BP devices exhibit 10^3 switching cycles under UV-A and UV-B illuminations without any significant decay in performance. However, ambient exposed devices show stability for more than 2 weeks, which can be further improved by surface treating with an imidazolium-based ionic liquid^[14] (Section S3, Supporting Information).

Furthermore, few-layer BP optoelectronic devices are fabricated on flexible polyethylene naphthalate (PEN) foil to demonstrate that these devices are also feasible to realize and operate effectively on flexible platforms for wearable electronics (Section S8, Supporting Information). The few-layer BP device

on PEN foil exhibits same photoresponse characteristics (i.e., positive photocurrent under 280 nm and negative photocurrent under 365 nm illumination) as on SiO_2/Si , which shows that the photoresponse of BP under UV illumination is independent of substrate (as discussed in Section S8 in the Supporting Information).

2.4. Optically Stimulated Synapses

Optical stimulation of excitatory and inhibitory synaptic activities in biological neurons is well established in neuroscience.^[57–59] Positive photoresponse of our few-layer BP devices (under 280 nm illumination) mimics excitatory action potential and negative photoresponse (under 365 nm) imitates inhibitory action potential, analogous to the neuronal activities triggered by optical stimuli in biological neurons. As such, few-layer BP renders mimicry of different synaptic functions in biological neurons and light-sensitive cells, such as retinal ganglion cells.

In a neuronal synapse (Figure 5a), stimuli-induced action potentials result in either excitatory postsynaptic current (EPSC) or inhibitory postsynaptic current (IPSC) that translate to strengthening and weakening of the synaptic connection, respectively. In the recently reported artificial photonic synapses,^[24,60] one of the two synaptic action potentials is imitated by applying electrical signals on their gate terminal, which hampers the realization of a low-power and all-optical neuro-morphic system. However, by utilizing positive and negative photocurrents of our BP devices under distinct wavelengths of UV, both excitatory and inhibitory action potentials can be imitated without the application of additional electrical signals on their gate terminal. As such, here we employ short optical pulses as stimulation spikes to induce positive and negative photocurrents in BP under distinct wavelengths of the UV and mimic both EPSC and IPSC (Figure 5b). Furthermore, we employ this unique photoresponse to optically imitate memory behavior (such as spike-rate-dependent plasticity (SRDP)) and Hebbian learning rule (such as spike-time-dependent plasticity (STDP)) in our few-layer BP synaptic devices.

Based on the retention time of sensory information, psychological memory behavior can be classified into short-term memory (STM) and long-term memory (LTM), where through consecutive rehearsal processes, the level of the memory can be changed. Our few-layer BP synaptic devices show a slower recovery of photocurrent after exposure to 280 nm illumination (as compared to 365 nm), which can be attributed to the persistent photocurrent in BP (Section S6, Supporting Information).^[38,61–63] This indicates that the BP synaptic devices exhibit LTM behavior under 280 nm and STM under 365 nm stimulation spikes. Figure 5c shows an increase in normalized EPSC as a function of the number of excitatory presynaptic optical spikes (of 280 nm with pulse width of 200 ms, power density of 2 mW cm^{-2} , and rate of 2.5 Hz). This suggests that the consecutive excitatory rehearsal stimulations result in the consolidation of memory and lead to a psychological *learning* experience defined by a simple exponential function

$$\gamma = \gamma_0 + B \cdot \exp(N/\tau_1) \quad (6)$$

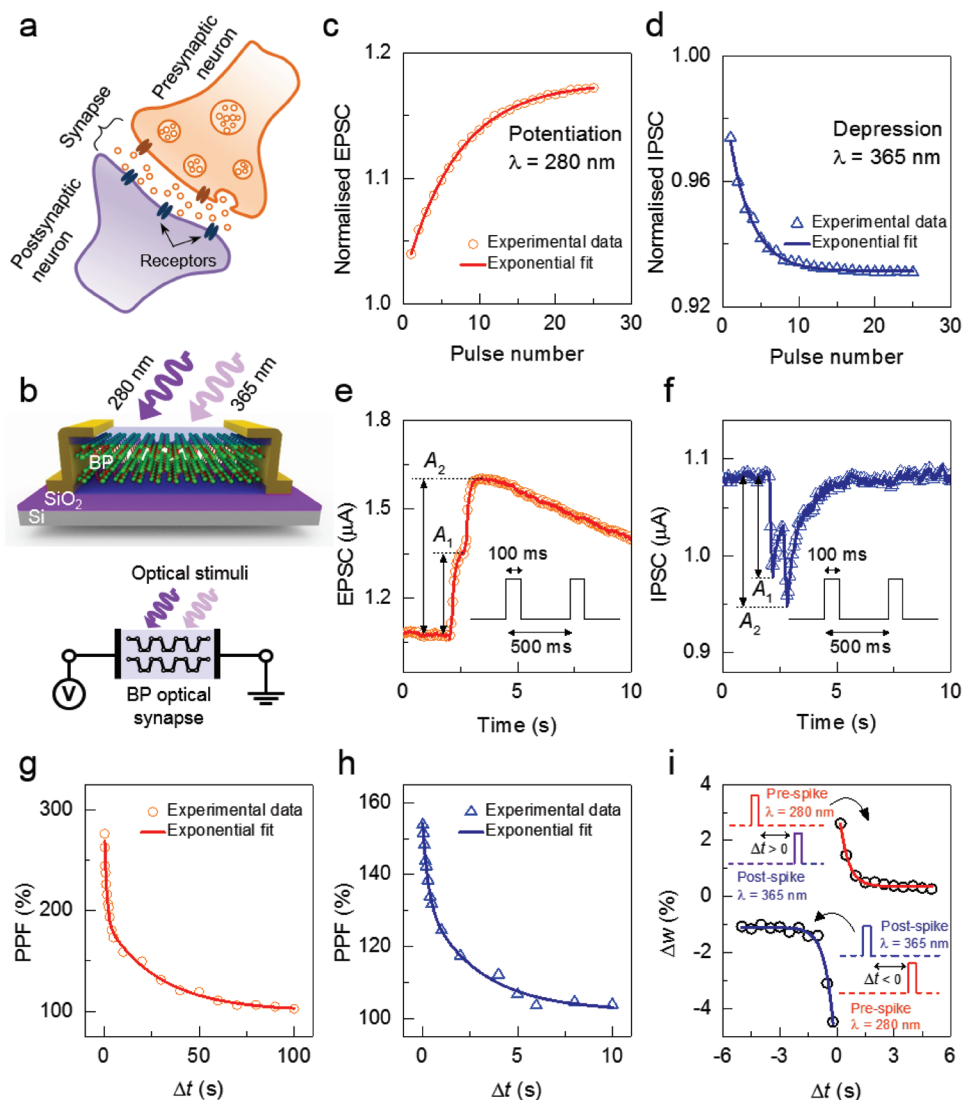


Figure 5. Optoelectronic few-layer BP synapses. a) A schematic representation of a biological synapse. b) A schematic demonstration of a few-layer BP optoelectronic synapse where excitation of optical stimuli with wavelengths of 280 and 365 nm induces potentiation and depression, respectively. Lower panel of (b) represents an equivalent of the BP optoelectronic synapse and our experimental setup to imitate synaptic functions. c) Normalized EPSC and d) normalized IPSC as a function of number of presynaptic optical spikes with pulse width of 200 ms, power density of 2 mW cm^{-2} , and rate of 2.5 Hz. The change in e) EPSC and f) IPSC in response to the pair of presynaptic optical pulses with time interval (Δt) of 500 ms and pulse width of 100 ms. A_1 and A_2 represent the change in postsynaptic current at first and second spikes, respectively. PPF index as a function of Δt between pairs of g) excitatory and h) inhibitory pulses. i) The synaptic weight (conductance) change (Δw) of the BP optoelectronic synapse as a function of time variation (Δt) in pre- and postsynaptic optical spikes. Inset: schematic of the pulses applied to imitate spike-time-dependent plasticity.

where N is the number of presynaptic spikes, B is initial facilitation magnitude in learning process, γ_0 is resting facilitation magnitude, and τ_1 is the learning (calculated to be 6.97 by fitting experimental data in Figure 5c). On the other hand, Figure 5d shows a decay in the normalized IPSC under inhibitory optical spikes (of 280 nm with pulse width of 200 ms, power density of 2 mW cm^{-2} , and rate of 2.5 Hz), which can be correlated to the Ebbinghaus' *forgetting* curve.^[64] The decay phenomenon of IPSC is fitted with an exponential function^[65,66]

$$\gamma = \gamma_0 + B \cdot \exp(-N/\tau_2) \quad (7)$$

where τ_2 is the *forgetting* rate (calculated to be 2.94 by fitting experimental data in Figure 5d). The imitation of brain-like

stimulation rate-dependent *learning* and *forgetting* processes (i.e., SRDP) in our BP synaptic devices by optical stimulation renders the capability of such optical synapses for artificial intelligence.

In a biological synapse, when two presynaptic spikes, separated by a short period of time, stimulate consecutively, then the change in postsynaptic weight is larger for the second spike. This induces dynamic synaptic plasticity known as paired-pulse facilitation (PPF).^[67] However, the magnitude of the second change is determined by the time interval between two consecutive spikes, such that a smaller time interval results in a larger change. The EPSC and IPSC induced by two successive excitatory and inhibitory optical pulses (with similar pulse

width of 100 ms, time interval of 500 ms, and power intensity of 2 mW cm⁻²) are shown in Figure 5e,f, respectively. Herein, change in both EPSC and IPSC is higher for the second optical pulse, imitating PPF phenomenon in our few-layer BP synaptic devices. The PPF index—ratio between amplitudes of postsynaptic currents induced by the second spike (A_2) and first spike (A_1)—is extracted and plotted as a function of time interval (Δt) between consecutive spikes in Figure 5g,h, respectively. These experimental PPF indexes can be fitted by the double exponential function given by

$$\gamma = \gamma_0 + B_1 \cdot \exp(-\Delta t/\tau_1) + B_2 \cdot \exp(-\Delta t/\tau_2) \quad (8)$$

where Δt is time interval between two consecutive optical pulses, B_1 and B_2 are facilitation magnitudes, and τ_1 and τ_2 are fast and slow decay times of the exponential function, respectively, calculated to be 1.2 and 28.7 s by fitting experimental data in Figure 5g and 0.3 and 2.8 s by fitting experimental data in Figure 5h. In a biological synapse, PPF is caused by the residual Ca²⁺ ion concentration left by first spike in the presynaptic neuron, which increases total Ca²⁺ ion level after the second spike. The residual Ca²⁺ ions exhibit exponential decay after the first spike, which causes lesser change in postsynaptic current when the time interval between the two spikes increases.^[67] Similarly, in our few-layer BP synaptic devices, PPF can be explained by the recombination of photogenerated carriers (i.e., relaxation time). At the end of the first optical pulse, electron–hole pairs start to recombine. If second optical pulse is exposed after a short time interval, the photogenerated electrons will not have enough time to recombine completely and charge carriers generated by the second pulse are augmented, which consequently induces PPF in the few-layer BP. On the other hand, if the second optical spike occurs with time interval larger than relaxation time, then photocurrent has similar magnitude to the first optical spike. This suggests that paired pulses with short time interval induce higher PPF index while it saturates at 100% for paired pulses with time interval equal to or higher than relaxation time.

To optically imitate the Hebbian learning rule via the paired STDP protocol, the synaptic weight (conductance of the BP channel, Δw) is determined by timing difference (Δt) and stimulation order of pre- and postsynaptic spikes. Figure 5i shows the optical implementation of STDP on our few-layer BP optoelectronic synaptic devices where short optical pulses of 280 nm (with pulse width of 200 ms and power intensity of 1 mW cm⁻²) as presynaptic spikes and 365 nm (with pulse width of 200 ms and power intensity of 4.2 mW cm⁻²) as postsynaptic spikes are excited to define asymmetric STDP. The percentage change in synaptic weight (Δw) versus the relative spike timing (Δt) can be fitted with exponential functions

$$\Delta w = \begin{cases} A_+ \cdot e^{(\Delta t/\tau_+)}, & \Delta t > 0 \\ A_- \cdot e^{(\Delta t/\tau_-)}, & \Delta t < 0 \end{cases} \quad (9)$$

where A_+/A_- are the scaling factors and τ_+/τ_- are the time constants for positive and negative Δt , respectively. The values calculated by data fitting for A_+/A_- are 3.4/–4.8 and for τ_+/τ_- are 0.44/–0.45 ms. It is worth mentioning that the recently reported optoelectronic devices employ a combination of electrical and

optical pulses to imitate such synaptic functions.^[22,24,60,68,69] However, our few-layer BP devices use only short optical pulses to mimic synaptic potentiation/habituation and fundamental neuronal functions (such as SRDP and STDP). Such a demonstration of optically imitating memory behavior and dynamic synaptic plasticity presents the potential of few-layer BP synaptic devices for the development of future photonic neuromorphic circuits and synthetic sensory organs, such as artificial retina.

2.5. Optoelectronic Digital Logic Operations

Scalable optoelectronic devices capable of performing logic computation with optical signals are highly desired for future applications because light renders ultrafast computational speed due to high bandwidth, low crosstalk, and ultralow power consumption. In this context, we exploit the opposing-polarity photoresponse of few-layer BP under different UV wavelengths to demonstrate an optoelectronic logic element. Figure 6a shows a schematic illustration of an integrated 2-bit optoelectronic exclusive OR (XOR) logic gate where 365 and 280 nm wavelengths act as input A and input B, respectively, for two serially connected BP devices. In our optical input–electronic output logic devices, output digital states are defined as the change in output current (ΔI) corresponding to a defined threshold. For XOR logic operation, the conditions for both optical inputs are set to induce similar magnitude of ΔI as stated in the inset of Figure 6a. The time trace of ΔI for 2-bit XOR operation (Figure 6b) shows that when both optical inputs are low [0–0] or high [1–1], the output ΔI does not increase/decrease compared to the defined threshold and retains a low level [0] (depicted by a shaded region and defined in the inset table of Figure 6a). On the other hand, the output ΔI changes the magnitude to high [1] when either of the two inputs is high, exhibiting an optical XOR logic operation.

Figure 6c shows a schematic illustration of a 2-bit optoelectronic OR/ADDER logic operation where the binary optical input signals are added to provide an output that is an analog equivalent to the digital sum. Figure 6d shows the time trace of ΔI for OR/ADDER logic operation for different input configurations where same 365 nm wavelength is illuminated for both input A and input B. Interestingly, magnitude of the photoresponse almost doubles when both inputs are high, which can be associated with the summation of photogenerated charge carriers. In this integrated device configuration, OR/ADDER logic operation can also be performed by illuminating 280 nm wavelength as input A and input B. In the future, the high-fidelity optical OR/ADDER logic operation can be extended to perform more complex operations (such as optoelectronic digital-to-analog convertor) by fabricating multiple integrated devices.

Since our BP devices exhibit positive photoresponse under shorter UV wavelengths (≤ 302 nm) and negative photoresponse under longer UV and visible wavelengths (365 and 455 nm, respectively), selection of any two wavelengths for an application can result in comparatively different magnitudes of photocurrent without affecting the capability to execute that application. Similarly, due to the intrinsic anisotropic optical absorbance of BP,

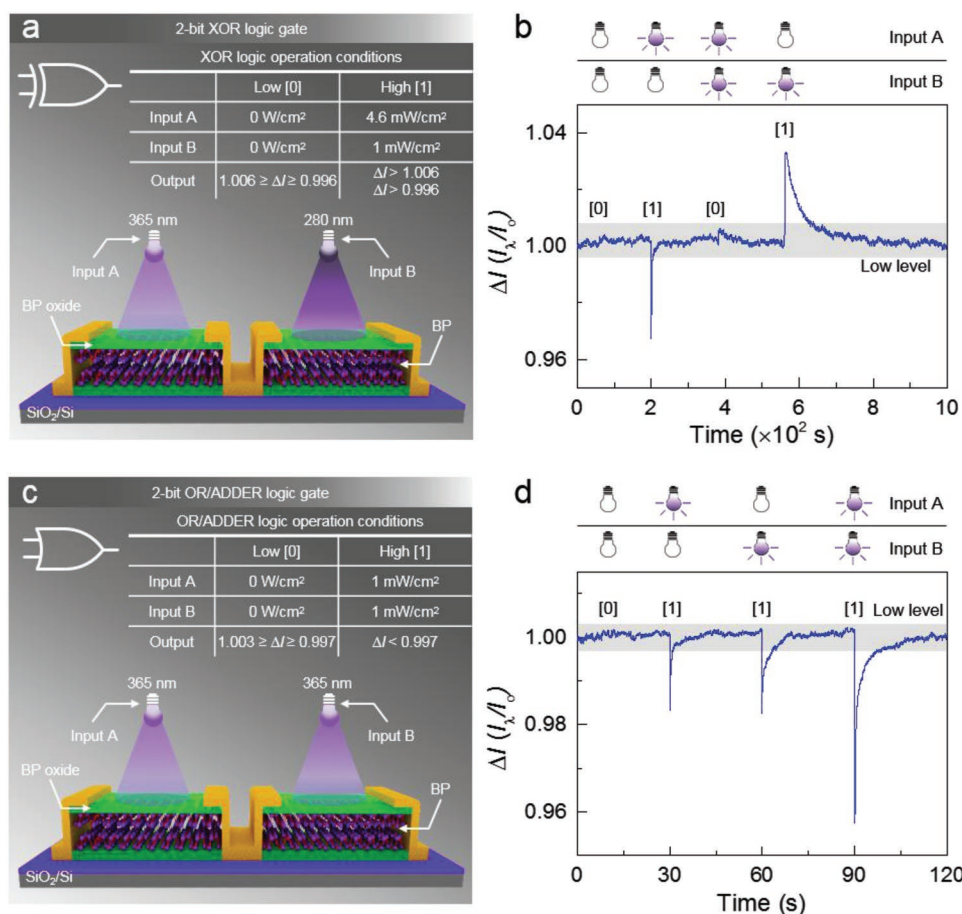


Figure 6. Optoelectronic digital logic operations. a) A schematic illustration of two serially integrated few-layer BP devices on a rigid SiO₂/Si substrate to perform 2-bit optoelectronic XOR logic operation. Excitation wavelengths of 365 and 280 nm with different incident power density are used as optical input signals on input A and input B, respectively, inducing similar magnitude in the change in output current. Inset table lists conditions for optoelectronic XOR logic operation. b) The change in output current (ΔI) versus time for different input configurations. The shaded region represents the current level where output is regarded as low [0] and is defined in inset table of (a). c) A schematic illustration of an integrated device performing 2-bit optoelectronic OR/ADDER logic operation. Same excitation wavelength of 365 nm is illuminated as input A and input B. Inset table lists conditions for OR/ADDER logic operation. d) Output response for different input A–B configurations. In both (a) and (b), the output current is measured under a constant 50 mV bias.

the magnitude of photocurrent is higher for polarized light along armchair direction than zigzag. As such, regardless of the light's polarization direction, the capability of our BP devices to exhibit a unique combination of positive and negative photoresponse for multifunctional applications remains unchanged.

3. Conclusion

In summary, our work has shown an innovative concept in revealing a unique photoresponse in BP. This work establishes an ability that can be exploited for a dynamic range of optoelectronic applications. The underpinning phenomenon of this photoresponse is investigated in detail using a series of experimental characterizations and detailed DFT simulations. Collectively, these show that the dissociation of ambient oxygen on BP surface introduces localized charge trap sites resulting in a negative photocurrent under 365 nm illumination, while ambient hydrogen molecules split under 280 nm and passivate the

oxygen sites inducing a positive photoresponse. This opposing-polarity photoresponse of BP is utilized to demonstrate three distinct applications. These include the ability of the proposed optoelectronic devices to selectively distinguish between UV-A and UV-B radiations, optical imitation of synaptic learning and forgetting processes, and integrated Boolean logic operations. In addition to these application examples, it is shown that optical characteristics are independent of the substrate material rendering adoptability of the BP optoelectronic devices for flexible and wearable electronics. As such, this demonstration highlights a pathway of defect engineering that can be extended to other 2D materials to anticipate their rich chemical/physical functionality for multidisciplinary applications.

4. Experimental Section

Device Fabrication: Layered BP flakes were obtained via polydimethylsiloxane-assisted micromechanical exfoliation of a commercial

bulk BP crystal (Smart Elements) onto rigid SiO₂ (300 nm)/Si and flexible polyethylene naphthalate and polyimide substrates. Electron beam lithography and photolithography were used to pattern electrodes on the selected BP flakes with different thicknesses ranging from ≈5.7 to ≈45 nm. The metal electrodes Cr/Au (5/70 nm) and Ti/Au (5/70 nm) were then deposited on the developed patterns using electron beam evaporation. Finally, the lift-off in acetone was carried out to reveal the required metallic contact pads for microprobes and electrical measurement.

AFM and Optical Characterizations: AFM topographic scans of the exfoliated BP flakes were conducted on a Dimension-Icon AFM in ScanAsyst mode. The Raman spectra were obtained by using a Horiba LabRAM Evolution micro-Raman system equipped with 9 mW, 532 nm laser (0.5 μm lateral resolution, 0.25 s exposure) and a 50× objective.

Transmission Electron Microscopy: BP flakes were transferred onto the lacey carbon grids. For cross-sectional analysis of BP devices, thin lamellae were prepared by focused ion beam using a FEI Scios DualBeam FIBSEM system. Then, TEM characterizations were carried out using a JEOL 2100F scanning transmission electron microscope with attached Tridium Gatan image filter, operating at 80 kV acceleration voltage. For EELS data analysis, power law fits were used for P-L and O-K pre-edge background corrections where the influence of nearby peaks and plural scattering were removed by selecting narrow signal windows.

Electrical and Optoelectronic Measurements: The electrical measurements were conducted using a Keithley 4200SCS semiconductor parameter analyzer and Agilent 2912A source meter. All measurements were performed under dark conditions with exposure to only the target illumination wavelengths. The field-dependent carrier mobilities (μ) were extracted from the equation $\mu = [L/(W \cdot C_{ox} \cdot V_{DS})](dI_{DS}/dV_{GS})$, where dI_{DS}/dV_{GS} is the transconductance, L is the channel length, W is the channel width, C_{ox} is the SiO₂ capacitance (calculated as 115 μF m⁻¹), and V_{DS} is the drain-source voltage.

For optoelectronic measurements, commercial light-emitting diodes with illumination wavelengths of 280 and 365 nm (Thorlabs, Inc.) were used as excitation sources. The illumination power was calibrated by a commercial UV-enhanced silicon photodetector (Newport Corporation). The excitation frequency and pulse width of the light sources were controlled by a programmable Arduino-Uino microcontroller board.

Thermal treatment of BP was conducted in a controlled environmental chamber (Linkam LTS420 probe stage) with a constant flow of pure (99.999%) Ar. To minimize the ambient degradation of BP without affecting its photoresponse, a recently reported chemical sequestration technique based on 1-butyl-3-methylimidazolium tetrafluoroborate ionic liquid was used (Section S3, Supporting Information).^[14]

DFT Simulations: To obtain the atomic and electronic structures of the phosphorene, spin-unrestricted DFT calculations were performed with the SIESTA code^[70] using the generalized gradient approximation for the exchange-correlation function as developed by Perdew, Burke, and Ernzerhof.^[71] The SIESTA code used basis sets comprised of numerical atomic orbitals, and approximated the atomic potential in terms of Troullier–Martins^[72] norm-conserving pseudopotentials. The auxiliary basis used a real-space mesh with a kinetic energy cutoff of 500 Ry, and the basis functions were radially confined using an energy shift of 0.005 Ry.^[70] Full atomic relaxation was allowed until the forces on the atoms were less than 0.01 eV Å⁻¹. The size of the k-point space was 3 × 3 × 1 for all structures considered.

UV-Vis Absorbance of BP: The UV-vis absorbance profiles of an ambient exposed BP flake before and after annealing were measured by CRAIC 20/30 XL UV-vis microspectrophotometer.

Supporting Information

Supporting Information is available from the Wiley Online Library or from the author.

Acknowledgements

This work was performed in part at the Micro Nano Research Facility (MNRF) at RMIT University in the Victorian Node of the Australian National Fabrication Facility. The authors acknowledge the facilities and technical support of the staff at MNRF and the RMIT Microscopy and Microanalysis Research Facility. The computational work was supported by the Multi-modal Australian Science Imaging and Visualisation Environment (MASSIVE), and was undertaken with the assistance of resources and services from the National Computational Infrastructure (NCI), and supported by resources provided by the Pawsey Supercomputing Centre with funding from the Australian Government and the Government of Western Australia. The authors also gratefully acknowledge Prof. S. Russo (School of Science, RMIT University) and Dr. S. Nawaz (Quantum Nanoelectronics Laboratory, UC Berkeley) for their support. The authors acknowledge support from the Australian Research Council (ARC) for personnel and project support (DP130100062), fellowships (DE160100023, FT140101285, and FT130101337), and infrastructure (LE0882246 and LE0989615) support.

Conflict of Interest

The authors declare no conflict of interest.

Keywords

black phosphorus, defect engineering, negative photocurrent, optoelectronics

Received: March 7, 2019

Revised: June 9, 2019

Published online:

- [1] J. Qiao, X. Kong, Z. X. Hu, F. Yang, W. Ji, *Nat. Commun.* **2014**, *5*, 4475.
- [2] H. Liu, A. T. Neal, Z. Zhu, Z. Luo, X. Xu, D. Tománek, P. D. Ye, *ACS Nano* **2014**, *8*, 4033.
- [3] Y. Zhou, M. Zhang, Z. Guo, L. Miao, S.-T. Han, Z. Wang, X. Zhang, H. Zhang, Z. Peng, *Mater. Horiz.* **2017**, *4*, 997.
- [4] S. C. Dhanabalan, J. S. Ponraj, Z. Guo, S. Li, Q. Bao, H. Zhang, *Adv. Sci.* **2017**, *4*, 1600305.
- [5] L. Li, Y. Yu, G. J. Ye, Q. Ge, X. Ou, H. Wu, D. Feng, X. H. Chen, Y. Zhang, *Nat. Nanotechnol.* **2014**, *9*, 372.
- [6] V. Tran, R. Soklaski, Y. Liang, L. Yang, *Phys. Rev. B* **2014**, *89*, 235319.
- [7] J. Lu, J. Yang, A. Carvalho, H. Liu, Y. Lu, C. H. Sow, *Acc. Chem. Res.* **2016**, *49*, 1806.
- [8] T. Ahmed, S. Balendhran, M. N. Karim, E. L. H. Mayes, M. R. Field, R. Ramanathan, M. Singh, V. Bansal, S. Sriram, M. Bhaskaran, S. Walia, *npj 2D Mater. Appl.* **2017**, *1*, 1.
- [9] S. Walia, Y. Sabri, T. Ahmed, M. R. Field, R. Ramanathan, A. Arash, S. K. Bhargava, S. Sriram, M. Bhaskaran, V. Bansal, S. Balendhran, *2D Mater.* **2017**, *4*, 015025.
- [10] W. Gaoxue, J. S. William, P. Ravindra, P. K. Shashi, *2D Mater.* **2016**, *3*, 025011.
- [11] A. Favron, E. Gaufres, F. Fossard, A. L. Phaneuf-L'Heureux, N. Y. Tang, P. L. Levesque, A. Loiseau, R. Leonelli, S. Francoeur, R. Martel, *Nat. Mater.* **2015**, *14*, 826.
- [12] M. T. Edmonds, A. Tadich, A. Carvalho, A. Ziletti, K. M. O'Donnell, S. P. Koenig, D. F. Coker, B. Ozyilmaz, A. H. Neto, M. S. Fuhrer, *ACS Appl. Mater. Interfaces* **2015**, *7*, 14557.
- [13] A. Castellanos-Gomez, L. Vicarelli, E. Prada, J. O. Island, K. L. Narasimha-Acharya, S. I. Blanter, D. J. Groenendijk,

- M. Buscema, G. A. Steele, J. V. Alvarez, H. W. Zandbergen, J. J. Palacios, H. S. J. van der Zant, *2D Mater.* **2014**, 1, 025001.
- [14] S. Walia, S. Balendhran, T. Ahmed, M. Singh, C. El-Badawi, M. D. Brennan, P. Weerathunge, M. N. Karim, F. Rahman, A. Russell, J. Duckworth, R. Ramanathan, G. E. Collis, C. J. Lobo, M. Toth, J. C. Kotsakidis, B. Weber, M. Fuhrer, J. M. Dominguez-Vera, M. J. S. Spencer, I. Aharonovich, S. Sriram, M. Bhaskaran, V. Bansal, *Adv. Mater.* **2017**, 29, 1700152.
- [15] S. Kuriakose, T. Ahmed, S. Balendhran, V. Bansal, S. Sriram, M. Bhaskaran, S. Walia, *2D Mater.* **2018**, 5, 032001.
- [16] C. Elbadawi, R. T. Queralt, Z.-Q. Xu, J. Bishop, T. Ahmed, S. Kuriakose, S. Walia, M. Toth, I. Aharonovich, C. J. Lobo, *ACS Appl. Mater. Interfaces* **2018**, 10, 24327.
- [17] Z. Guo, S. Chen, Z. Wang, Z. Yang, F. Liu, Y. Xu, J. Wang, Y. Yi, H. Zhang, L. Liao, P. K. Chu, X. F. Yu, *Adv. Mater.* **2017**, 29, 1703811.
- [18] X. Ren, Z. Li, Z. Huang, D. Sang, H. Qiao, X. Qi, J. Li, J. Zhong, H. Zhang, *Adv. Funct. Mater.* **2017**, 27, 1606834.
- [19] Z. Lin, B. R. Carvalho, E. Kahn, R. Lv, R. Rao, H. Terrones, M. A. Pimenta, M. Terrones, *2D Mater.* **2016**, 3, 022002.
- [20] M. Singh, D. Jampaiah, A. E. Kandjani, Y. M. Sabri, E. Della Gaspera, P. Reineck, M. Judd, J. Langley, N. Cox, J. van Embden, E. L. H. Mayes, B. C. Gibson, S. K. Bhargava, R. Ramanathan, V. Bansal, *Nanoscale* **2018**, 10, 6039.
- [21] J. Xiong, J. Di, J. Xia, W. Zhu, H. Li, *Adv. Funct. Mater.* **2018**, 28, 1801983.
- [22] Y. Wang, Z. Lv, J. Chen, Z. Wang, Y. Zhou, L. Zhou, X. Chen, S. T. Han, *Adv. Mater.* **2018**, 30, 1802883.
- [23] R. A. John, F. Liu, N. A. Chien, M. R. Kulkarni, C. Zhu, Q. Fu, A. Basu, Z. Liu, N. Mathews, *Adv. Mater.* **2018**, 30, 1800220.
- [24] S. Qin, F. Wang, Y. Liu, Q. Wan, X. Wang, Y. Xu, Y. Shi, X. Wang, R. Zhang, *2D Mater.* **2017**, 4, 035022.
- [25] S. Wu, J. Han, R. A. Vleugels, R. Puett, F. Laden, D. J. Hunter, A. A. Qureshi, *Br. J. Cancer* **2014**, 110, 1855.
- [26] J. A. Parrish, K. F. Jaenicke, R. R. Anderson, *Photochem. Photobiol.* **1982**, 36, 187.
- [27] W. Zou, A. González, D. Jampaiah, R. Ramanathan, M. Taha, S. Walia, S. Sriram, M. Bhaskaran, J. M. Dominguez-Vera, V. Bansal, *Nat. Commun.* **2018**, 9, 3743.
- [28] N. Mao, J. Tang, L. Xie, J. Wu, B. Han, J. Lin, S. Deng, W. Ji, H. Xu, K. Liu, L. Tong, J. Zhang, *J. Am. Chem. Soc.* **2016**, 138, 300.
- [29] F. Xia, H. Wang, Y. Jia, *Nat. Commun.* **2014**, 5, 4458.
- [30] H. Yuan, X. Liu, F. Afshinmanesh, W. Li, G. Xu, J. Sun, B. Lian, A. G. Curto, G. Ye, Y. Hikita, Z. Shen, S. C. Zhang, X. Chen, M. Brongersma, H. Y. Hwang, Y. Cui, *Nat. Nanotechnol.* **2015**, 10, 707.
- [31] C. Biswas, F. Gunes, D. L. Duong, S. C. Lim, M. S. Jeong, D. Pribat, Y. H. Lee, *Nano Lett.* **2011**, 11, 4682.
- [32] J. Miao, B. Song, Q. Li, L. Cai, S. Zhang, W. Hu, L. Dong, C. Wang, *ACS Nano* **2017**, 11, 6048.
- [33] L. Huang, W. C. Tan, L. Wang, B. Dong, C. Lee, K. W. Ang, *ACS Appl. Mater. Interfaces* **2017**, 9, 36130.
- [34] S. Liu, N. Huo, S. Gan, Y. Li, Z. Wei, B. Huang, J. Liu, J. Li, H. Chen, *J. Mater. Chem. C* **2015**, 3, 10974.
- [35] J. Y. Wu, Y. T. Chun, S. Li, T. Zhang, J. Wang, P. K. Shrestha, D. Chu, *Adv. Mater.* **2018**, 30, 1705880.
- [36] K. L. Utt, P. Rivero, M. Mehboudi, E. O. Harriss, M. F. Borunda, A. A. Pacheco SanJuan, S. Barraza-Lopez, *ACS Cent. Sci.* **2015**, 1, 320.
- [37] J. D. Wood, S. A. Wells, D. Jariwala, K.-S. Chen, E. Cho, V. K. Sangwan, X. Liu, L. J. Lauhon, T. J. Marks, M. C. Hersam, *Nano Lett.* **2014**, 14, 6964.
- [38] J. Wu, G. K. W. Koon, D. Xiang, C. Han, C. T. Toh, E. S. Kulkarni, I. Verzhbitskiy, A. Carvalho, A. S. Rodin, S. P. Koenig, G. Eda, W. Chen, A. H. C. Neto, B. Özyilmaz, *ACS Nano* **2015**, 9, 8070.
- [39] A. Ziletti, A. Carvalho, P. E. Trevisanutto, D. K. Campbell, D. F. Coker, A. H. Castro Neto, *Phys. Rev. B* **2015**, 91, 085407.
- [40] A. Ziletti, A. Carvalho, D. K. Campbell, D. F. Coker, A. H. Castro Neto, *Phys. Rev. Lett.* **2015**, 114, 046801.
- [41] P. Srivastava, K. P. S. S. Hembram, H. Mizuseki, K.-R. Lee, S. S. Han, S. Kim, *J. Phys. Chem. C* **2015**, 119, 6530.
- [42] J. Lu, J. Wu, A. Carvalho, A. Ziletti, H. Liu, J. Tan, Y. Chen, A. H. Castro Neto, B. Özyilmaz, C. H. Sow, *ACS Nano* **2015**, 9, 10411.
- [43] D. W. Boukhvalov, A. N. Rudenko, D. A. Prishchenko, V. G. Mazurenko, M. I. Katsnelson, *Phys. Chem. Chem. Phys.* **2015**, 17, 15209.
- [44] T. Ahmed, S. Balendhran, M. N. Karim, E. L. H. Mayes, M. R. Field, R. Ramanathan, M. Singh, V. Bansal, S. Sriram, M. Bhaskaran, S. Walia, *npj 2D Mater. Appl.* **2017**, 1, 1.
- [45] D. Wang, D. Han, X. B. Li, S. Y. Xie, N. K. Chen, W. Q. Tian, D. West, H. B. Sun, S. B. Zhang, *Phys. Rev. Lett.* **2015**, 114, 196801.
- [46] D. Wang, D. Han, D. West, N.-K. Chen, S.-Y. Xie, W. Q. Tian, V. Meunier, S. Zhang, X.-B. Li, *npj Comput. Mater.* **2019**, 5, 1.
- [47] D. Wang, X.-B. Li, D. Han, W. Q. Tian, H.-B. Sun, *Nano Today* **2017**, 16, 30.
- [48] S. Yang, A. Kim, J. Park, H. Kwon, P. T. Lanh, S. Hong, K. J. Kim, J. W. Kim, *Appl. Surf. Sci.* **2018**, 457, 773.
- [49] S. Fan, H. Hei, C. An, W. Pang, D. Zhang, X. Hu, S. Wu, J. Liu, *J. Mater. Chem. C* **2017**, 5, 10638.
- [50] M. H. Jeong, D. Kwak, H. S. Ra, A. Y. Lee, J. S. Lee, *ACS Appl. Mater. Interfaces* **2018**, 10, 19069.
- [51] X. Gong, M. Tong, Y. Xia, W. Cai, J. S. Moon, Y. Cao, G. Yu, C.-L. Shieh, B. Nilsson, A. J. Heeger, *Science* **2009**, 325, 1665.
- [52] M. Buscema, D. J. Groenendijk, S. I. Blanter, G. A. Steele, H. S. van der Zant, A. Castellanos-Gomez, *Nano Lett.* **2014**, 14, 3347.
- [53] M. Huang, M. Wang, C. Chen, Z. Ma, X. Li, J. Han, Y. Wu, *Adv. Mater.* **2016**, 28, 3481.
- [54] M. M. Furchi, D. K. Polyushkin, A. Pospischil, T. Mueller, *Nano Lett.* **2014**, 14, 6165.
- [55] M. Tan, C. Hu, Y. Lan, J. Khan, H. Deng, X. Yang, P. Wang, X. Yu, J. Lai, H. Song, *Small* **2017**, 13, 1702024.
- [56] X. Chen, X. Lu, B. Deng, O. Sinai, Y. Shao, C. Li, S. Yuan, V. Tran, K. Watanabe, T. Taniguchi, D. Naveh, L. Yang, F. Xia, *Nat. Commun.* **2017**, 8, 1672.
- [57] J.-J. Pang, F. Gao, S. M. Wu, *J. Neurosci.* **2003**, 23, 6063.
- [58] E. S. Boyden, F. Zhang, E. Bamberg, G. Nagel, K. Deisseroth, *Nat. Neurosci.* **2005**, 8, 1263.
- [59] A. C. Thompson, P. R. Stoddart, E. D. Jansen, *Curr. Mol. Imaging* **2014**, 3, 162.
- [60] H. K. He, R. Yang, W. Zhou, H. M. Huang, J. Xiong, L. Gan, T. Y. Zhai, X. Guo, *Small* **2018**, 14, 1.
- [61] M. B. Erande, M. S. Pawar, D. J. Late, *ACS Appl. Mater. Interfaces* **2016**, 8, 11548.
- [62] S. Kuriakose, T. Ahmed, S. Balendhran, G. E. Collis, V. Bansal, I. Aharonovich, S. Sriram, M. Bhaskaran, S. Walia, *Appl. Mater. Today* **2018**, 12, 244.
- [63] T. Ahmed, S. Kuriakose, E. L. H. Mayes, R. Ramanathan, V. Bansal, M. Bhaskaran, S. Sriram, S. Walia, *Small* **2019**, 15, 1900966.
- [64] T. Ohno, T. Hasegawa, T. Tsuruoka, K. Terabe, J. K. Gimzewski, M. Aono, *Nat. Mater.* **2011**, 10, 591.
- [65] Z. Q. Wang, H. Y. Xu, X. H. Li, H. Yu, Y. C. Liu, X. J. Zhu, *Adv. Funct. Mater.* **2012**, 22, 2759.
- [66] R. Yang, K. Terabe, Y. Yao, T. Tsuruoka, T. Hasegawa, J. K. Gimzewski, M. Aono, *Nanotechnology* **2013**, 24, 384003.
- [67] D. Debanne, N. C. Guérineau, B. H. Gähwiler, S. M. Thompson, *J. Physiol.* **1996**, 491, 163.
- [68] S. Dai, X. Wu, D. Liu, Y. Chu, K. Wang, B. Yang, J. Huang, *ACS Appl. Mater. Interfaces* **2018**, 10, 21472.
- [69] M. Lee, W. Lee, S. Choi, J. W. Jo, J. Kim, S. K. Park, Y. H. Kim, *Adv. Mater.* **2017**, 29, 1700951.
- [70] M. S. José, A. Emilio, D. G. Julian, G. Alberto, J. Javier, O. Pablo, S.-P. Daniel, *J. Phys.: Condens. Matter* **2002**, 14, 2745.
- [71] J. P. Perdew, K. Burke, M. Ernzerhof, *Phys. Rev. Lett.* **1996**, 77, 3865.
- [72] N. Troullier, J. Martins, *Solid State Commun.* **1990**, 74, 613.